

Influence of top contact noble metals on leakage current properties of epitaxial BaTiO₃ film capacitors

Wei Zhang^{1,3} · Jun Ouyang² · Limin Kang⁴ · Hongbo Cheng² · Qian Yang² · Fangren Hu^{1,3}

Received: 27 June 2015 / Accepted: 24 August 2015 / Published online: 29 August 2015
© Springer Science+Business Media New York 2015

Abstract Dielectric properties, ferroelectric hysteresis loops, and leakage current characteristics of an epitaxial BaTiO₃ (BTO) film were investigated with La_{0.5}Sr_{0.5}CoO₃ as bottom electrode and the different noble metal as top electrodes (Au, Ag and Pt, which were deposited on the same surface of a BTO film). The dielectric constants, dielectric loss, leakage currents and ferroelectric loops all exhibited the top-electrode-dependent behavior, which can be attributed to the different interface state. The *J–V* characteristics were analyzed with various transportation mechanisms in detail. Regardless of the top electrode materials, the leakage current characteristics were described by a modified Schottky contact model for all BTO film capacitors. It was proved that large space charge densities were the main contribution to the slim hysteresis loops. The potential of these interface charge dominated BTO film heterostructures in the application of high energy density storage capacitors was also demonstrated.

1 Introduction

The ferroelectric thin-film capacitors are structured in an electrode layer—ferroelectric layer—electrode layers sandwich. The contact type between the electrodes and ferroelectric film is important for the transport phenomena in this tri-layer system [1], thus the electrodes play an important role in a capacitor grown on a single-crystal substrate. The electrode materials can be classified into two general groups. The first group consists of noble metals such as Pt, Au, Ir and Ru, while the second is the conducting perovskite oxide electrodes. Usually, La_{0.5}Sr_{0.5}CoO₃ (LSCO), La_{0.5}Sr_{0.5}MnO₃ (LSMO), SrRuO₃ (SRO), LaNiO₃ (LNO), YBa₂Cu₃O_{7–x} (YBCO), and Ca_{0.5}Sr_{0.5}RuO₃ (CSR) are of considerable interest since the similar crystal structure and lattice constants with many perovskite ferroelectric materials. LSCO has a pseudo-cubic perovskite structure with a resistivity of 90 μΩ·cm, and a lattice parameter of 3.835 Å at room temperature. The LSCO as the bottom electrode can be found in the literature [2–4], but there is few report considering the fabrication of LSCO layer as bottom electrode with 90° off-axis RFMS technology, which induces excellent crystal quality of the films deposited on it. The corresponding geometry was shown in Fig. 1a.

It is well documented that the electrical properties and its characterization of the ferroelectric thin films are strongly depended on the ferroelectric-electrode interface. The interface states must be well understood to optimize the design of thin film-based devices. The formation of an interface state including strain state, defects and parameters associated with space-charge-transport, is affected by a number of factors such as electrode material, electrode microstructure, and deposition parameters. Furthermore, the interface state will greatly affect the leakage current,

✉ Wei Zhang
chanway@njupt.edu.cn

✉ Jun Ouyang
ouyangjun@sdu.edu.cn

¹ School of Optoelectronic Engineering, Nanjing University of Posts and Telecommunications, Nanjing 210023, China

² Key Laboratory for Liquid-Solid Structure Evolution and Processing of Materials (Ministry of Education), School of Materials Science and Engineering, Shandong University, Jinan 250061, China

³ Peter Grunberg Research Center, Nanjing University of Posts and Telecommunications, Nanjing 210003, China

⁴ Shandong Research and Design Institute Ceramics CO., LTD, Zibo 255031, China

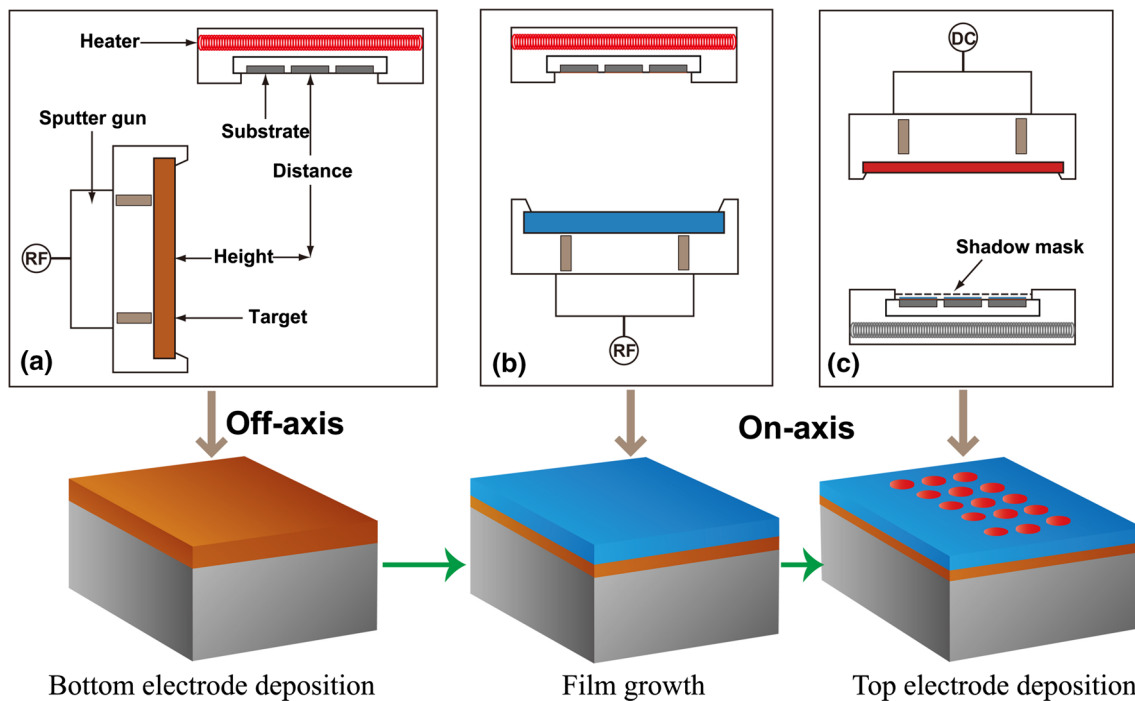


Fig. 1 (Color online) Schematic of the preparation process of BaTiO₃ films heterostructure. **a** La_{0.5}Sr_{0.5}CoO₃ bottom electrode layer was deposited by 90° off-axis RF magnetron sputtering.

dielectric permittivity, polarization and phase-transition temperature of the ferroelectric films. Many researches focus on the bottom electrode effects on the physical properties of the ferroelectric thin films [5–7]. Capacitors with oxide electrodes have higher leakage current density than those with Pt electrodes, which needs to be lowered prior to considering them for DRAM applications [5]. The conduction mechanism is bulk-limited Poole–Frenkel emission in IrO₂/BST/IrO₂ film capacitors, while interface-limited Schottky emission in Pt/BST/Pt, and the dielectric constant is decreased by a half [6]. These work suggested that the bottom electrode has a great influence on the electrical properties, however, few study has focused on that of the top electrode.

In addition, top electrodes dependences of various physical properties in PZT, PT and La-doped PT ferroelectric capacitors have been occasionally reported [1, 8, 9]. However, it is not clear whether or not these relationships derived from the above Pb-based films are application to BTO ones. BTO is one of the most intensively studied lead-free ferroelectric perovskites and technologically interesting materials due to its many useful electrical properties as well as drastic variations in the structure characteristics in the vicinity of a para-to-ferroelectric phase transformation. Particularly, compared with BTO single crystals, BTO-based thin films have received much attention in these years for excellent structural perfection and their important applications in ultrahigh density memory devices [10] and microsystems

b BaTiO₃ ferroelectric layer was deposited by on-axis RF magnetron sputtering. **c** Noble metal top electrodes were fabricated by on-axis DC magnetron sputtering

technology [11], such as memories (FeRAM, DRAMs, RAM) [12–15], multilayer capacitors [16], microwave devices and micro-electromechanical systems (MEMS) [17]. So attention is needed to be put on the importance of the electrode-BTO film interface for these important applications and to study the breakdown phenomena in ferroelectric capacitors with different metal electrodes, especially for memory devices [15, 18].

In this paper, to clarify the top contact effect on the electric properties, especially the interface-charge-transport properties, of BTO thin films, different noble metals (Au, Ag, Pt) as top electrode were used in BTO ferroelectric film heterostructure. Then the dielectric properties, hysteresis loops, leakage current properties and top interface contact states were comprehensively studied with the experimental characterization and theoretical analysis. The present study addresses the influence of various top noble metal electrodes on the electric properties of high quality epitaxial BTO films. This work is important for understanding the material characteristics and designing the equivalent circuits of electronic devices based on BTO film heterostructures.

2 Experimental

A 50-nm-thick La_{0.5}Sr_{0.5}CoO₃ (LSCO) bottom electrode layer was deposited on (100) SrTiO₃ (STO) substrate from an LSCO ceramic target by using a 90° off-axis radio

frequency magnetron sputtering (RFMS) technique. Then 500-nm-thick BTO ferroelectric film layer sputtered from a BTO ceramic target by on-axis RFMS technique. Figure 1 shows the preparation process, and the off-axis and on-axis RFMS geometries for BTO/LSCO/STO heterostructures are schematically shown in Fig. 1a, b. The off-axis technique is capable of producing epitaxial thin films with smooth surfaces [19], and also can use a single composite target instead of multi-elemental sources, which is a considerable advantage in heterostructure and multilayer deposition [20]. Before these (100) STO substrates ($10 \times 10 \times 0.5 \text{ mm}^3$) were loaded into the growth chamber, they were successively ultrasonic cleaned in acetone, ethanol and deionized water. To clean up residual contaminants, a plasma bombardment process was applied to these substrates in the pre-sputtering vacuum chamber. The detailed deposition parameters can be seen elsewhere [7, 21]. After the deposition processes of BTO and LSCO layers were finished, different noble metal top electrodes (circular, 200 μm diameter) of Pt, Au and Ag were deposited at room temperature onto the same surface of a BTO film by direct current sputtering by using a shadow mask (Fig. 1c). No post-annealing was performed in order to retain the stress state of the as-grown films.

The crystal microstructure and lattice spacing of BTO and LSCO thin film layers were investigated by using X-ray diffraction 2θ scans in a commercial Rigaku Dmax-rc diffractometer equipped with a Ni-filter, and Φ -scans in a high power (18 kW) IP crystal X-ray diffractometer equipped with R-Axis-spider. Cu K_α radiation source was employed in both diffractometers. The ferroelectric hysteresis loops and leakage current characteristic were measured via Radiant Technologies RT6000 ferroelectric test system at room temperature. The dielectric properties were tested by using a high precision digital bridge (QuadTech 7600plus).

3 Results and discussion

3.1 Crystal structures

The crystalline structure and orientation of the films were analyzed by conventional X-ray 2θ scans. Figure 2 shows the XRD θ - 2θ measurement of the BTO films deposited on STO (100) substrate. Only the $\{00l\}$ diffraction peaks were observed in the thin film, and the full-width at half-maximum (FWHM) value of the (001) peak was only 0.349° . While the inset, the Φ -scan pattern for BTO (101) reflection shows four strong reflection peaks equally separated by 90° , indicating that the surface normal of the BTO film matches with the fourfold symmetry of the LSCO/STO. Namely, it is a cube-on-cube hetero-epitaxial

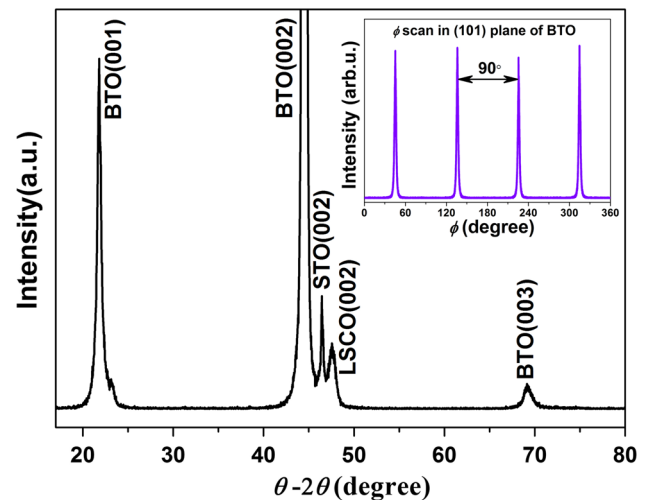


Fig. 2 (Color online) X-ray diffraction pattern for BaTiO_3 thin films deposited in pure argon growing atmosphere on (100)-oriented SrTiO_3 substrates with $\text{La}_{0.5}\text{Sr}_{0.5}\text{CoO}_3$ as bottom electrode. Inset shows Φ scan for BaTiO_3 film showing in-plane orientation symmetry

growth for BTO film on LSCO/STO substrate, and the in-plane epitaxial relationship between them was $[100]_{\text{BTO}} // [100]_{\text{LSCO/STO}}$. It can be explained by good interface lattice matching and the interface energy minimization during the film growth process. Similarity of lattice parameters between STO ($a = 3.905 \text{ \AA}$) and LSCO ($a = 3.835 \text{ \AA}$) helps to orient the grain growth of the deposited film. On the other hand, a method of 90° off-axis single-target RFMS (see Fig. 1a) was employed to deposit LSCO layer, which helped to reduce the damage from the sputtering species to the substrate-film interface. Together with a low surface free energy of $\{100\}$ planes in perovskites, the high temperature off-axis sputtering technique successfully promoted the epitaxial growth of a (100) LSCO layer on STO, which also helped to exhibit (001) epitaxial BTO thin films.

3.2 Dielectric properties

Figure 3 shows the frequency dependence (0.5 kHz–2 MHz) of dielectric constant and loss tangent of BTO film capacitors with various top electrodes. For all BTO film capacitors, the dielectric constant decreases and loss tangent increases with increasing frequency, respectively. They display strong frequency dispersion behaviors especially when the frequency exceeded 200 kHz. It can be explained by the dielectric relaxation processes, which is analogous to bulk ferro-ceramic [7]. There are several possible sources contributing to such a behavior in the BTO/LSCO heterostructure, such as the dielectric dispersion of LSCO bottom electrode, the existence of an interfacial barrier layer and compositional diffusion [22], etc. It

has been proposed that the dispersion behavior can be suppressed by using noble metal instead of conductive oxide as bottom electrode [7, 23]. Specifically, the dielectric constants ϵ_r at 1 kHz are 230, 282 and 264 for Au/BTO/LSCO, Ag/BTO/LSCO, and Pt/BTO/LSCO, respectively. The values of loss tangent $\tan\delta$ are similar ($\sim 3\%$) at low frequency. The largest dielectric constant at low and medium frequencies for Ag/BTO/LSCO is suggested to originate from the better top contact interface states, such as the thinnest interface layer and depletion layer, the least structural defects and the better electrode characteristics for Ag (Table 1: the lowest resistivity ρ , the smallest electronegativity χ and electron affinity E). However, at higher frequency (>200 kHz), it seems that the BTO film with Ag top electrode exhibits the largest decrease speed for dielectric constant and increase speed for dielectric loss tangent. This maybe arises from the strongest diffusion behavior of Ag in three metals.

3.3 Leakage currents

Figure 4a shows the measured current density of the BTO films for Au, Ag and Pt top electrodes in a given voltage range (J - E curves). It is found that the measured leakage current density at room temperature of the BTO film

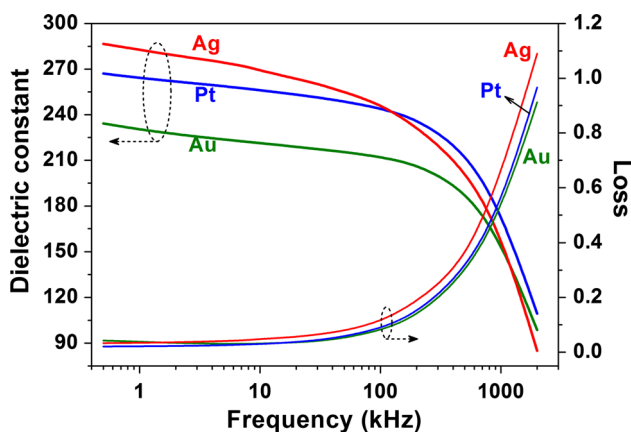


Fig. 3 (Color online) Frequency dependence of the dielectric constant and loss tangent of BTO film capacitors with different top electrode: Au, Ag and Pt

Table 1 Electronegativity χ , electron affinity E , and resistivity ρ of the noble metal top electrodes, the evaluated values for static dielectric constant ϵ_s , effective space charge density N_e (the superscript p and n denote the positive polarity and negative polarity, respectively), potential barrier on the negative polarity Φ_B^{TE} (top electrode side) for epitaxial BTO film with Au, Ag and Pt as top electrodes

Noble metals	χ (eV)	E (eV)	ρ ($\mu\Omega$ cm)	$\epsilon_s(\times\epsilon_0)$	N_e^p (10^{19} cm $^{-3}$)	N_e^n (10^{19} cm $^{-3}$)	Φ_B^{TE} (± 0.03 eV)
Au	2.54	2.31	2.4	230	0.15	1.49	0.888
Ag	1.93	1.31	1.58	282	1.68	1.88	0.868
Pt	2.28	2.12	10.6	264	0.40	0.36	0.814

capacitor with Au electrodes is the lowest and Pt is the largest. Although Pt/BTO/LSCO/STO has a larger current than others, all BTO film capacitors show very low leakage current density on the order of 10^{-6} A/cm 2 . The corresponding schematic of electrical performance test was present in the inset, and all three kinds of noble metals were grown on the same surface of a BTO film. The same BTO film exhibits different leakage current properties only just with different top electrodes. It is suggested that the top electrode materials and the interface states play important roles in the leakage current behavior.

To identify the leakage mechanism of our BTO film heterstructures, the experimental leakage current data were re-plotted according to various transportation mechanisms. Table 2 presents expressions of leakage current density and the linear relationships of J - E for space-charge-limited conduction (SCLC), Poole-Frenkel (PF) emission, Ionic conduction (IC), Schottky emission (SE) and Fowler-Nordheim (FN) tunneling. The last two conductions are interface dominated mechanisms, whereas the others are bulk-limited mechanisms. If the leakage current is controlled by the SCLC mechanism, the leakage current density can be divided into several different regions dominated by $\log J \propto \alpha \log E$, where $\alpha = 1$ in the Ohm's law region, $\alpha = 2$ in the trap-free square law region, and $\alpha > 2$ in the trap-filled limit region [24]. As shown in Fig. 5a, the slopes extracted from $\log J \propto \log E$ curves (only shown the negative voltage side here, the similar results for the positive side, the same treatment to all pictures in Fig. 5) of BTO film capacitors with top electrodes of Au and Pt are 1.04 and 0.85, respectively. Capacitor with Ag electrode can be divided into two regions with slopes of 0.89 (low field) and 1.37 (high field). J is approximately linear with E , especially for sample with Au top electrode, which indicated that the SCLC mechanism cannot be ruled out here. In Fig. 5b-d, no linear relations were found in PF, IC and FN modes with $\ln(J/E) \propto E^{1/2}$, $\ln(J) \propto E$, and $\ln(J/E^2) \propto 1/E$, respectively. So the dominant leakage behaviors of BTO film capacitors do not conform to these three transportation mechanisms.

The last one is the interface-limited Schottky emission which originates from metal-semiconductor Schottky contacts and the Schottky barrier will be formed at the inter-

face of the metal and the semiconductor. If the interface of the noble metal and BTO film is Schottky contact, a straight line should be observed in the plot of $\ln(J) \propto E^{1/2}$. As shown in Fig. 5e, the results showed linear $\ln(J) \propto E^{1/2}$ relationships for all BTO film capacitors. It maybe demonstrates that Schottky emission is also a controlling factor. It is well known that Schottky emission is a commonly observed phenomenon for ferroelectric materials with a metallic electrode. Although a ferroelectric can be considered as a simple semiconductor, the interface state of them is different due to the presence of polarization charge in ferroelectric. In order to better understand the Schottky theory and its application in the ferroelectric interface, a modified Schottky model must be addressed.

The Schottky emission based on the Schottky barrier at the interface of the metal and the semiconductor can be

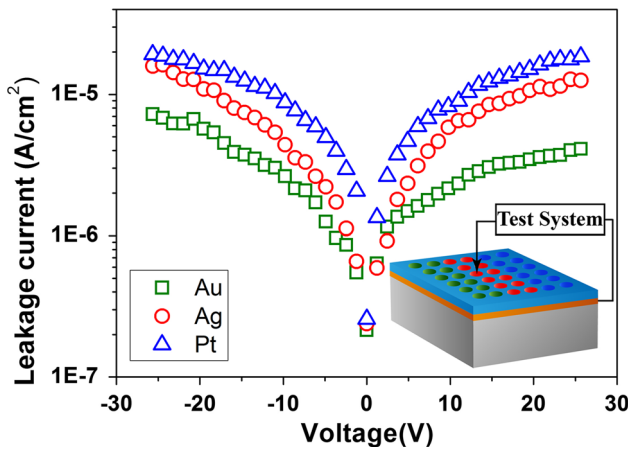


Fig. 4 (Color online) leakage current characteristics of all studied BTO film capacitors. The inset shows the configurations for electrical testing in Au (Ag, Pt)/BTO/LSCO/STO heterostructure

described by: $J_{SE} = A^*T^2 \cdot \exp\left[\frac{-q(\Phi_b - \psi_{SE})}{kT}\right]$ where $\psi_{SE} = \sqrt{qE/4\pi\epsilon_d}$ is the lowering of the barrier height due to the image force interaction and the applied field, A^* denotes the effective Richardson–Dushman constant, Φ_b is the interfacial Schottky barrier height, ϵ_d , q and k are the dynamic dielectric constant, the electronic charge and Boltzmann constant, respectively. In the case of ferroelectric, we must consider the contribution from polarization charge. Then the electric field is given by $E = \sqrt{\frac{2qN_e(V+V_{bi} \pm \Delta V_{bi})}{\epsilon_s} \pm \frac{P(V)}{\epsilon_s}}$ [21] where ΔV_{bi} is the change in built-in potential due to the effects from ferroelectric polarization charge at a reverse biased ferroelectric-electrode contact, ϵ_s is the static dielectric constant, the plus and minus signs are for the negative and positive polarization charges. If we redefine a new built-in potential $V_{bi}^p = V_{bi} \pm \Delta V_{bi}$, the new linear relationship of J – E can be written as $\ln(J) = b(V + V_{bi}^p)^{1/4}$ and the slope of $b = \frac{q}{kT} \sqrt[4]{\frac{q^3 N_e}{8\pi^2 \epsilon_s^2 \epsilon_d}}$ where N_e is effective charge density in the depletion layer.

As shown in Fig. 5f, our results also showed linear $\ln(J) \propto (V + V_{bi}^p)^{1/4}$ relationships for all BTO film capacitors. It indicated that Schottky emission is main controlling factor for our BTO film heterostructures. V_{bi}^p and slope b were obtained by linear fitting, if dielectric constants ϵ_s and ϵ_d were known, the effective charge density N_e can be estimated. The static dielectric constants $\epsilon_s(\times\epsilon_0)$ were found to be 230, 282 and 264 (at 1 kHz) in Fig. 3, respectively. The dynamic dielectric constants $\epsilon_d(\times\epsilon_0)$ were estimated to be 17 [25]. Then the space charge densities N_e were calculated and the results were presented in Table 1. All BTO film capacitor structures showed a large space charge density on the

Table 2 Leakage current expressions for various conduction mechanisms

Conduction mechanism	Leakage current expression	J – E linear relationship
Ohms	$J = n_0 q \mu E$	$J \propto E$
SCLC	$J = \frac{9\epsilon_0 \epsilon_r \mu E^2}{8d}$	$J \propto E^2$
P–F	$J = A_1 E \exp\left(\frac{-q(\phi_B - \sqrt{qE/\pi\epsilon_0\epsilon_r})}{kT}\right)$	$\ln(J/E) \propto E^{1/2}$
Ionic	$J = 2qN\lambda v \exp\left(\frac{-U}{kT}\right) \exp\left(\frac{q\lambda E}{2kT}\right)$	$\ln(J) \propto E$
F–N	$J = A_3 E^2 \exp\left(\frac{-\phi_D \sqrt{2m\phi_{eff}}}{\hbar q E}\right)$	$\ln(J/E^2) \propto \frac{1}{E}$
Schottky	$J = A_2 T^2 \exp\left(\frac{-q(\phi_B - \sqrt{qE/4\pi\epsilon_0\epsilon_r})}{kT}\right)$	$\ln(J) \propto E^{1/2}$
Modified Schottky	$J = A^* T^2 \exp\left(\frac{-q(\phi_B - \sqrt{qE/4\pi\epsilon_0\epsilon_r})}{kT}\right) E = \sqrt{\frac{2qN_e(V+V_{bi}^p)}{\epsilon_s} \pm \frac{P(V)}{\epsilon_s}}$	$\ln(J) \propto (V + V_{bi}^p)^{1/4}$

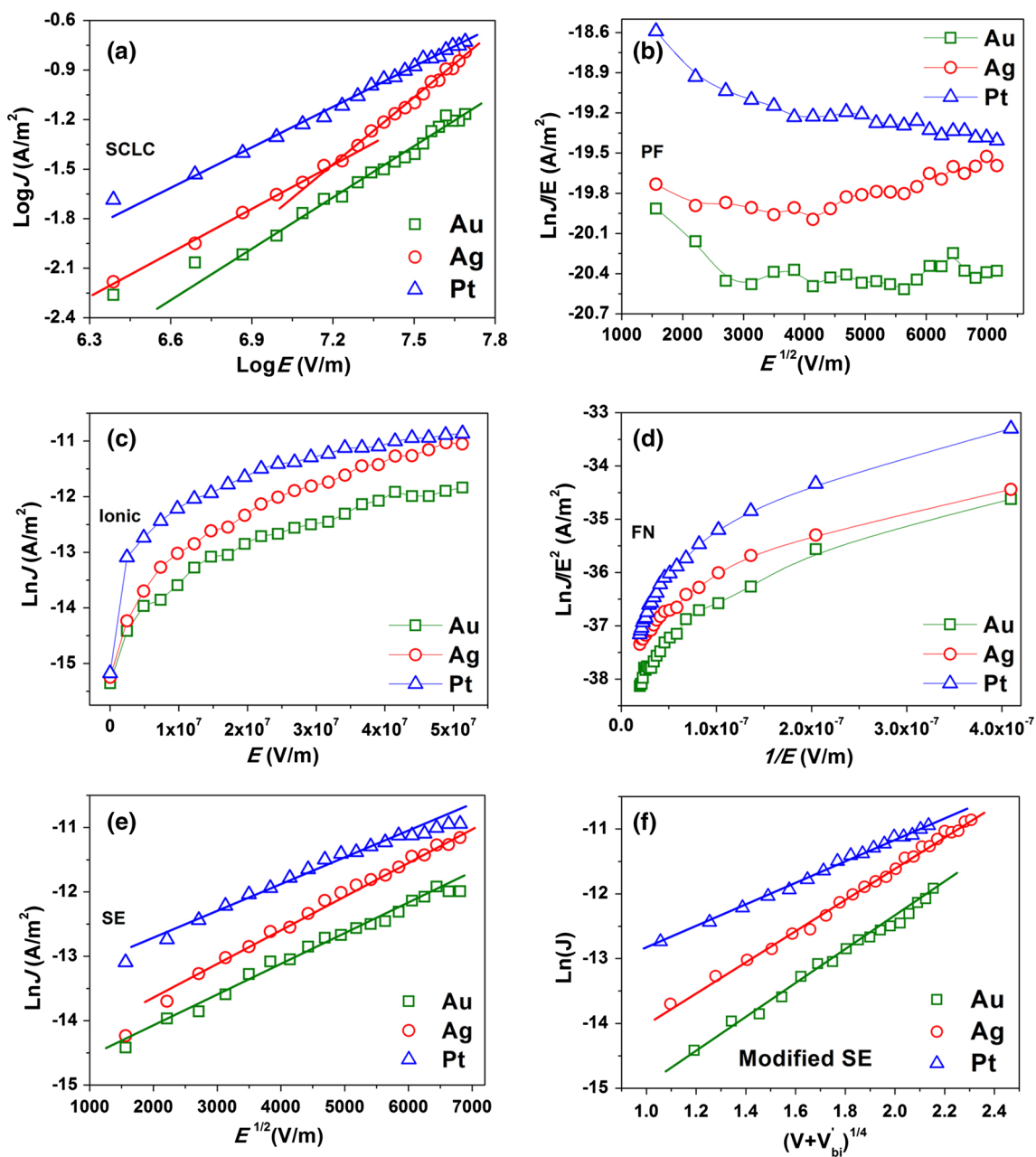


Fig. 5 (Color online) J – E relationships of the BTO film with different top noble metals. **a** $\log(J)$ versus $\log(E)$ characteristics, the lines are SCLC fittings; **b** $\ln(J/E)$ versus $E^{1/2}$ curves; **c** $\ln(J)$

versus E curves; **d** $\ln(J/E^2)$ versus $1/E$ curves; **e** $\ln(J)$ versus $E^{1/2}$ characteristics, the lines are Schottky emission fittings; **f** fitting of leakage current densities with modified Schottky contact model

order of 10^{19} cm^{-3} , which will significantly influence the electrical characteristics of a ferroelectric film structure [26]. If Richardson constant A^* was known, the J – V characteristic can be well simulated by using the potential barrier Φ_b as a fit parameter. A^* was assumed to be $310 \text{ A cm}^{-2} \text{ K}^{-2}$ here [21, 25], then the potential barrier can be obtained and the results were also presented in Table 1.

3.4 Hysteresis loops

P – V hysteresis curves of our BTO ferroelectric film capacitors with various top contact noble metal electrodes under the voltage of 80 V (about 1.6 MV/cm) are shown in Fig. 6. The remnant polarization ($2P_r$) of the BTO film with Au, Ag and Pt as top electrode are 7.3, 5.87 and 5.86, respectively, and the corresponding maximum polarization

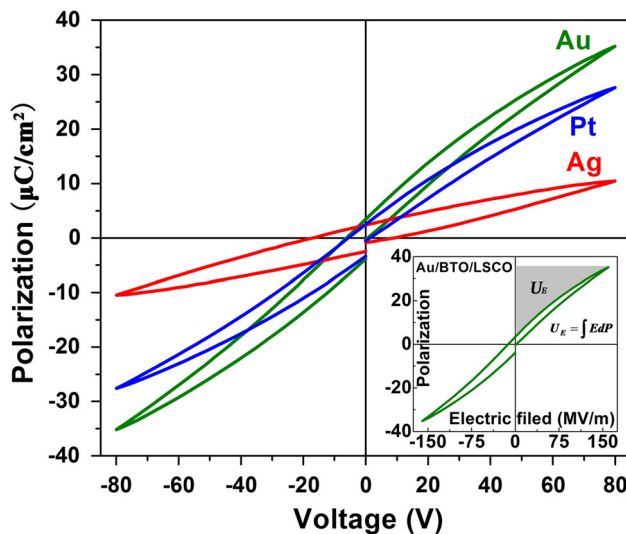


Fig. 6 (Color online) Hysteresis loops of BTO films with Au, Ag and Pt as top electrode. The inset was the demonstration of energy density of the Au/BTO/LSCO/STO heterostructure

(P_m) are 35.2, 10.47 and 27.62, respectively, much higher than the former. That is to say, all films showed the slim and tilted P - V loops. Such characteristics agreed well with our previous results about the space charge density. The high densities of the space charge density ($\sim 10^{19}$) revealed that our BTO film might be primarily responsible for the shape change of P - V loops. It was found that many possible factors will contribute to the shrink, tilt or disappearance of a P - V loop, such as reduction of the Curie temperature, large depletion charge density and the poly-domain structure [27, 28]. As shown in Fig. 6, the P - V loop of our BTO film with Ag as top contact metal has the largest tilting angle, which corresponds well with the largest charge density (Table 1). It further suggested that the charge density plays a dominant role for the ferroelectric characteristic. One possible application of BTO ferroelectric film capacitors with the slim P - E hysteresis loops is to provide high density storage of capacitive energy. As shown in the inset of Fig. 6, the shaded area represents the effective energy density of the BTO film. The energy density was calculated with the integral $U = \int_{PR}^{PM} E dP = 22.2 \text{ J/cm}^3$ with the applied field of 160 MV/m.

4 Conclusions

Conductive LSCO bottom electrode and BTO ferroelectric film were successively deposited on the (100) SrTiO₃ substrates by 90° off-axis and on-axis radio frequency magnetron sputtering, respectively. The XRD patterns reflected a pure perovskite phase and (001) epitaxial

orientation of the BTO film. Then the noble metal Pt, Au and Ag were deposited on the same surface of a BTO film as top electrodes. The $\epsilon - f$, $\epsilon - \tan \delta$, J - V and P - V behaviors of BTO film with these noble metals were investigated. With the same BTO film, the electric properties dependent on the different top metals. The top electrode dependence of dielectric constants and loss tangent showed the different value (at the same frequency) and the similar variation tendencies with frequency, which can be attributed to the different interface states. The leakage currents and ferroelectric loops also exhibited the top-electrode-dependence behavior. J - V characteristics were analyzed using various transportation mechanisms, including the possible control mechanisms, Schottky emission and SCLC. The leakage current characteristics for all BTO film capacitors were best described by a modified Schottky contact model. It was proved that the large space charge densities were the main contribution to the slim hysteresis loops.

Acknowledgments This work was supported by the National Natural Science Foundation of China (NSFC) (Grant Nos. 51002088, 91122024 and 61274121) and Jiangsu Province NSFC (Grant Nos. BK2012829 and BK20150842). Ouyang would also like to thank the Program for New Century Excellent Talents in University (State Education Ministry- SEM), Nano Projects of Soochow City (Grant No. ZXG201445), and the project sponsored by the Scientific Research Foundation (SRF) for the Returned Oversea Chinese Scholars (ROCS, SEM). Hu and Zhang would also like to thank the talent project of Nanjing University of Posts and Telecommunications (NUPTSF) (Grant Nos. NY212007 and NY214161).

References

1. L. Pintilie, L. Vrejoiu, D. Hesse, M. Alexe, J. Appl. Phys. **104**, 114101 (2008)
2. J. Ge, G. Pan, D. Remiens, Y. Chen, F. Cao, X. Dong, G. Wang, Appl. Phys. Lett. **101**, 112905 (2012)
3. B. Park, T. Noh, J. Lee, C. Kim, W. Jo, Appl. Phys. Lett. **70**, 1101–1103 (1997)
4. F. Chen, J. Cheng, S. Yu, Z. Meng, J. Mater. Sci. Mater. Electron. **21**, 514–518 (2010)
5. B. Nagaraj, S. Aggarwal, R. Ramesh, J. Appl. Phys. **90**, 375–382 (2001)
6. C.S. Hwang, B.T. Lee, C.S. Kang, J.W. Kim, K.H. Lee, H.J. Cho, H. Horii, W.D. Kim, S.I. Lee, Y.B. Roh, J. Appl. Phys. **83**, 3703–3713 (1998)
7. W. Zhang, L. Kang, M. Yuan, Q. Yang, J. Ouyang, J. Alloys Compd. **580**, 363–368 (2013)
8. J. Robertson, C.W. Chen, Appl. Phys. Lett. **74**, 1168–1170 (1999)
9. S.K. Dey, J.J. Lee, P. Alluri, Jpn. J. Appl. Phys. **34**, 3142–3152 (1995)
10. L.W. Martin, Y.H. Chu, R. Ramesh, Mater. Sci. Eng. R Rep. **68**, 89–133 (2010)
11. R. Ashiri, A. Nemat, M.S. Ghamsari, Ceram. Int. **40**, 8613–8619 (2014)
12. S. Nazarpour, E. Langenberg, O. Jamboisc, C. Ferrater, M.V. Garcia-Cuenca, M.C. Polo, M. Varela, Appl. Surf. Sci. **255**, 3618–3622 (2009)

13. K.J. Choi, M. Biegalski, Y.L. Li, A. Sharan, J. Schubert, R. Uecker, P. Reiche, Y.B. Chen, X.Q. Pan, V. Gopalan, L.Q. Chen, D.G. Schlom, C.B. Eom, *Science* **306**, 1005–1009 (2004)
14. A. Chanthbouala, A. Crassous, V. Garcia, K. Bouzehouane, S. Fusil, X. Moya, J. Allibe, B. Dlubak, J. Grollier, S. Xavier, C. Deranlot, A. Moshar, R. Rokschi, N.D. Mathur, M. Bibes, *Nat. Nanotechnol.* **7**, 101–104 (2012)
15. J.F. Scott, *Science* **315**, 954–959 (2007)
16. K. Iijima, T. Terashima, K. Yamamoto, K. Hirata, Y. Bando, *Appl. Phys. Lett.* **56**, 527–529 (1990)
17. Y. Guo, K. Suzuki, K. Nishizawa, T. Miki, K. Kat, *Acta Mater.* **54**, 3893–3898 (2006)
18. J.F. Scott, *Jpn. J. Appl. Phys.* **38**, 2272–2274 (1999)
19. C.B. Eom, J.Z. Sun, K. Yamamoto, A.F. Marshall, K.E. Luther, S.S. Laderman, T.H. Geballe, *Appl. Phys. Lett.* **55**, 595–597 (1989)
20. R.A. Rao, Q. Gan, C.B. Eom, Y. Suzuki, A.A. McDaniel, J.W.P. Hsu, *Appl. Phys. Lett.* **69**, 3911–3913 (1996)
21. W. Zhang, Y. Gao, L. Kang, M. Yuan, Q. Yang, H. Cheng, J. Ouyang, *Acta Mater.* **85**, 207–215 (2015)
22. T. Zhang, H. Ni, *Sensor. Actuat. A.-Phys.* **100**, 252–256 (2002)
23. L. Qiao, X. Bi, J. Alloys Compd. **477**, 560–564 (2009)
24. M.A. Lampert, P. Mark, *Current Injection in Solids* (Academic, New York, 1970)
25. R.R. Das, P. Bhattacharya, R.S. Katiyar, A.S. Bhalla, *Appl. Phys.* **92**, 6160–6164 (2002)
26. P. Zubko, D.J. Jung, J.F. Scott, *J. Appl. Phys.* **100**, 114112 (2006)
27. I.B. Misirlioglu, H.N. Cologlu, M. Yildiz, *J. Appl. Phys.* **111**, 064105 (2012)
28. A.M. Bratkovsky, A.P. Levanyuk, *Phys. Rev. B* **61**, 15042 (2000)